THE JOURNAL OF PHYSICAL CHEMISTRY A
A JOURNAL OF THE AMERICAN CHEMICAL SOCIETY

pubs.acs.org/JPCA

Article

Probing the Dipole-Bound State in the 9-Phenanthrolate Anion by Photodetachment Spectroscopy, Resonant Two-Photon Photoelectron Imaging, and Resonant Photoelectron Spectroscopy

Published as part of The Journal of Physical Chemistry virtual special issue "Daniel Neumark Festschrift".

Dao-Fu Yuan, Yue-Rou Zhang, Chen-Hui Qian, Yuan Liu, and Lai-Sheng Wang*

Cite This: *J. Phys. Chem. A* 2021, 125, 2967−2976

Read Online

ACCESS | Metrics & More | Article Recommendations | Supporting Information

ABSTRACT: Valence-bound anions with a dipolar core can support dipole-bound states (DBSs) below the electron detachment threshold. The highly diffuse DBS observed is usually of σ symmetry with an s-like orbital. Recently, a π-type DBS was observed experimentally in the 9-anthrolate anion ($9AT^-$) and it was shown to be stabilized due to the large anisotropic polarizability of the 9AT core. To confirm the general existence of π-DBS and its structural dependence, here we report an investigation of the 9-phenanthrolate anion ($9PT^-$), which has a different structure and lower symmetry than $9AT^-$. Photodetachment spectroscopy revealed a DBS 257 cm^{-1} below the detachment threshold of $9PT^-$ at 19 627 cm^{-1} (2.4334 eV). Resonant two-photon photoelectron imaging indeed showed a π symmetry for the DBS. Similar to that observed in $9AT^-$, the π-DBS in $9PT^-$ is also stabilized by the anisotropic polarizability of the 9PT core and accessed via nonadiabatic population transfer from the initially populated σ-DBS. Photodetachment spectroscopy unveiled nine above-threshold vibrational resonances of the DBS, resulting in nine highly non-Franck−Condon resonant photoelectron spectra by tuning the detachment laser to the vibrational resonances. The combination of photodetachment spectroscopy and resonant photoelectron spectroscopy allowed frequencies for nine vibrational modes of the 9-phenathroxy radical to be measured, including the six lowest frequency bending modes.

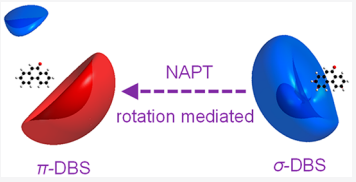

1. INTRODUCTION

Polar molecules with sufficiently large dipole moments can form highly diffuse dipole-bound anions.[1−5] Valence-bound anions with polar cores can possess dipole-bound excited states just below the electron detachment threshold,[6−13] similar to Rydberg states in neutral molecules. Dipole-bound states (DBSs) have been suggested as the "doorway" to the formation of valence-bound anions,[14−16] which is important in electron−molecule scattering, DNA damage by low-energy electrons, and anion formation in the interstellar medium.[17−21] Recently, DBSs have been exploited as a means to develop high-resolution resonant photoelectron spectroscopy (rPES),[22−27] which yields highly non-Franck−Condon photoelectron spectra via vibrational autodetachment and much richer spectroscopic information than afforded by conventional PES.

For a fixed dipole system, there can be an infinite number of bound DBSs above a critical dipole moment.[3,28] For such an electron−dipole system, the critical dipole moment is 1.62 D for the first bound DBS with a σ-type orbital,[29] and it is ∼9.64 D for the first π-type DBS.[3,28] On the other hand, for a freely rotating electron−dipole system, a larger dipole moment is required to support a DBS.[30,31] The critical dipole moment is shown empirically to be about 2.5 D for the lowest σ-type DBS.[1,4,32−34] A critical dipole moment higher than 4.5 D is required for the second σ-DBS with one additional node in the radial wave function.[3,35,36] By analogy, the critical dipole moment should be larger than 9.64 D for the first π-DBS. Compared with σ-DBSs, which have no angular nodes, π-DBSs have an angular node similar to a p-orbital. Experimentally, an electronically excited DBS above the lowest σ-DBS has not been observed, even for systems with a dipole moment as large as 6.2 D.[37] All the previous photoelectron imaging studies of DBSs have shown p-wave angular distributions, suggesting these DBSs consist of a σ-type orbital with no angular nodes.

Very recently, a π-type DBS was observed for the first time in the 9-anthrolate anion ($9AT^-$) using resonant two-photon detachment (R2PD) photoelectron imaging (see Figure S1 for the structure of $9AT^-$).[38] Even though the dipole moment of the 9AT neutral radical is only 3.6 D, the π-DBS was shown to be stabilized due to the large polarizability of 9AT in the direction perpendicular to the dipole axis (along the three phenyl rings, Figure S1). The population of the π-DBS was proposed to come from nonadiabatic coupling from the initially excited σ-DBS, being mediated by molecular rotation. The large in-plane polarizability of polycyclic aromatic

Received: February 20, 2021
Revised: March 23, 2021
Published: April 2, 2021

hydrocarbons (PAHs) provides ideal systems to examine how DBSs are influenced by polarization and electron correlation effects. In this article, we report an investigation of the 9-phenanthrolate anion ($9PT^-$, see structure in Figure 1a and Figure S1), which has the same size as $9AT^-$ ($C_{14}H_9O^-$) but has a different structure with lower symmetry. The 9-phenanthrol molecule is an alcohol derivative of phenanthrene, a common PAH, which can be produced from incomplete combustion of fossil fuels.[39] The 9-phenanthrol molecule was known for more than a century and it was recently found to be an inhibitor of a calcium-activated cation channel.[40] The 9PT radical, along with other aromatic-oxy radicals, may also be involved in soot formation during hydrocarbon combustion.[41] However, there is little known about the energetics and spectroscopy of the 9PT radical. Hence, obtaining energetic and spectroscopic information about the 9PT radical is another objective of the current study.

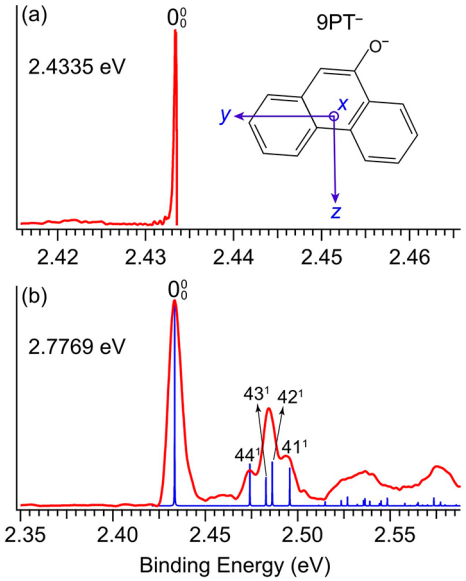

Figure 1. Nonresonant photoelectron spectra of $9PT^-$ at (a) 2.4335 eV and (b) 2.7769 eV. Calculated Franck−Condon factors, given as vertical lines in (b), are also shown for comparison. The inset in (a) shows the molecular structure of $9PT^-$ and the coordinates used.

High-resolution anion PES has been championed by the Neumark group using slow electron velocity-map imaging (SEVI),[42,43] which has been used to study a number of PAH-related radical species.[44−48] We have developed an experimental technique coupling electrospray ionization (ESI),[49] cryogenic ion cooling in a 3D Paul trap,[50] and high-resolution photoelectron imaging.[51] Using this third generation ESI-PES apparatus,[52] we have investigated DBSs as electronically excited states of valence-bound anions and employed vibrational autodetachment from DBSs to conduct rPES on a wide variety of cryogenically cooled anions,[22−27] including several PAH species.[43,53,54] In the present study, we report an investigation of cryogenically cooled $9PT^-$ using photodetachment spectroscopy (PDS), R2PD photoelectron imaging, and rPES. We observe a π-DBS in $9PT^-$ 257 cm^{-1} below its detachment threshold. The electron affinity (EA) of the 9PT radical is measured accurately to be 19 627 ± 3 cm^{-1} (2.4334 ± 0.0004 eV). Similar to that in $9AT^-$, the π-DBS in $9PT^-$ is also found to be stabilized by the anisotropic polarizability of 9PT and accessed via nonadiabatic population transfer from the initially populated σ-DBS. The combination of PDS and rPES has allowed vibrational frequencies for nine vibrational modes of 9PT to be measured, including the six lowest frequency bending modes.

2. EXPERIMENTAL AND COMPUTATIONAL METHODS

2.1. Photoelectron Imaging. The experiment was conducted using our third generation ESI-PES apparatus,[52] coupled with a cryogenically cooled 3D Paul trap[50] and a high-resolution photoelectron imaging system.[51] Briefly, the $9PT^-$ anions were formed by electrospray ionization of a 1 mM solution of 9-phenanthrol in a CH_3OH/H_2O mixed solvent (9/1 volume ratio) at a pH of ∼10 adjusted by adding a small amount of NaOH. Anions from the ESI source were guided into a cryogenically cooled Paul trap by a series of quadrupole and octupole ion guides. The ion trap was cooled to about 4.6 K by a two-stage closed cycle helium refrigerator. The anions were accumulated in the Paul trap and thermally cooled via collisions with a background gas consisted of ∼1 mTorr He/H_2 (4/1 in volume).[50] The rotational temperature of the cooled anions was estimated to be 30−35 K.[23,55] After being accumulated and cooled for 0.1 s, the anions were pulsed out at a 10 Hz repetition rate into the extraction zone of a time-of-flight mass spectrometer. The $9PT^-$ anions were selected by a mass gate and photodetached in the interaction zone of the imaging lens by a tunable dye laser. The detachment laser was operated at a repetition rate of 20 Hz to allow shot-by-shot background subtraction. Photoelectrons were projected onto a pair of 75 mm diameter microchannel plates coupled to a phosphor screen. The photoelectron images were captured by a charge-coupled-device camera and were inverse-Abel transformed using pBasex[56] and BASEX.[57] The photoelectron spectra were calibrated with the known spectra of Au^- at different photon energies. The electron kinetic energy (KE) resolution achieved was 3.8 cm^{-1} for electrons with 55 cm^{-1} KE and about 1.5% (ΔKE/KE) for electrons above 1 eV KE in the current experiment.[51]

2.2. Computational Methods. The molecular geometries in the ground and valence excited states of $9PT^-$ were optimized using the B3LYP functional[58−60] and the Def2-TZVPP basis set.[61,62] The vibrational frequency, polarizability, dipole moment, and EA of neutral 9PT were calculated on the same level of theory. The valence excited state of $9PT^-$ was then calculated at the anion's optimized geometry using time-dependent density functional theory (TD-DFT)[63−65] at the B3LYP/Def2-TZVPP level of theory. The dipole-bound excited electronic states were calculated using TD-DFT at the CAM-B3LYP/Def2-TZVPP+4s3p2d1f level of theory. We used the CAM-B3LYP functional[66] to better capture the long-range nature of the interaction between the excess electron and the neutral 9PT core. Additional 4s3p2d1f basis functions were added selectively to three carbon atoms in the molecule to accommodate the diffuse nature of the wave functions of the weakly bound states. The exponents of the diffuse functions and the three carbon atoms (circled in the structure) are given in Table S1. All calculations were performed using Gaussian 09.[67]

3. RESULTS

3.1. Nonresonant Photoelectron Spectra. Figure 1 shows the nonresonant photoelectron spectra of $9PT^-$ at two

https://doi.org/10.1021/acs.jpca.1c01563
J. Phys. Chem. A 2021, 125, 2967−2976

photon energies. In order to accurately measure the EA of the neutral 9PT radical, we took a spectrum at a photon energy very near the detachment threshold (Figure 1a). The sharp 0_0^0 transition defines an accurate EA of 19 627 ± 3 cm^{-1} (2.4334 eV ± 0.0004 eV) for 9PT. The spectrum shown in Figure 1b was taken at a higher photon energy, displaying a broader Franck−Condon region for the detachment transition from the ground state of $9PT^-$ to that of the 9PT radical. A Franck−Condon calculation was done, as compared with the experimental data in Figure 1b. The Franck−Condon factors were calculated using FC-LAB2 and the optimized geometries and computed vibrational frequencies at the B3LYP level (see Table S2).[68]

3.2. Photodetachment Spectroscopy. Our calculation yielded a dipole moment of 4.4 D for 9PT, suggesting that a DBS should exist below the detachment threshold of $9PT^-$. We scanned the detachment laser wavelength around the detachment threshold and monitored the total electron yield to obtain the photodetachment spectrum, as shown in Figure 2. A

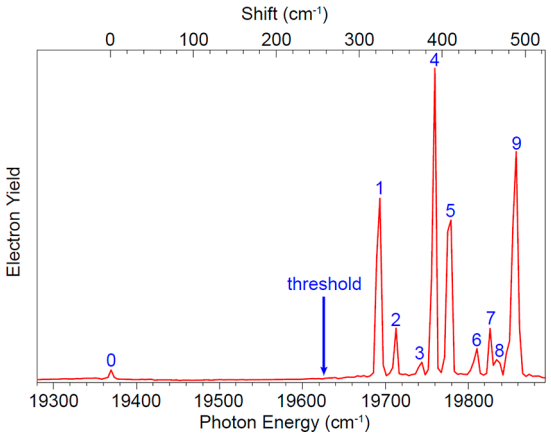

Figure 2. Photodetachment spectrum of $9PT^-$ by measuring the total electron yield as a function of photon energy near the detachment threshold, indicated by the arrow. Ten vibrational peaks are observed and labeled as 0−9.

series of sharp peaks (labeled as 0−9) were indeed observed, corresponding to the vibrational levels of the expected DBS. The arrow at 19 627 cm^{-1} denotes the position of the detachment threshold obtained from Figure 1a. The baseline above the threshold in Figure 2 represents contributions from single-photon nonresonant detachment processes. The weak peak below the threshold (peak 0) at 19 370 cm^{-1} (2.4016 eV) should correspond to the ground vibrational level of the DBS as a result of R2PD, similar to those observed previously.[34,69,70] The energy difference between the detachment threshold and peak 0 defines the binding energy of the DBS to be 257 ± 3 cm^{-1} (0.0319 ± 0.0004 eV). More prominently, the nine above-threshold peaks (1−9) in Figure 2 are due to single-photon excitations to vibrational levels of the DBS of $9PT^-$. These peaks are also known as vibrational Feshbach resonances and they are observed due to vibrational autodetachment. The wavelengths, photon energies, and assignments of the DBS vibrational peaks are given in Table 1.

3.3. R2PD Photoelectron Imaging. By tuning the detachment laser to the position of peak 0 in Figure 2, we obtained the R2PD photoelectron image and spectrum of $9PT^-$, as shown in Figure 3. This spectrum is similar to that of

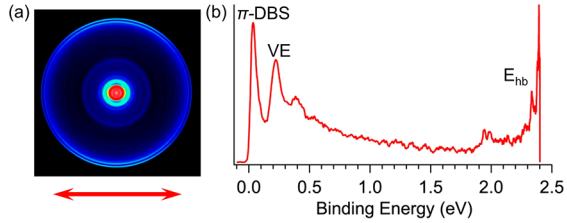

Figure 3. R2PD photoelectron image (a) and spectrum (b) of $9PT^-$ via the bound ground vibrational level of the DBS at 516.25 nm (19 370 cm^{-1}) corresponding to peak 0 in Figure 2. The double arrow below the image represents the laser polarization. Peaks labeled as VE and E_{hb} represent photoelectrons detached from a valence excited state and vibrational levels of the ground electronic state of $9PT^-$, respectively.

$9AT^-$ observed recently.[38] The low binding energy peak labeled as "π-DBS" represents direct R2PD from the DBS of $9PT^-$ corresponding to the outermost ring in the image (Figure 3a). Besides this expected sharp R2PD photoelectron peak, additional unexpected features were observed. A well-resolved and relatively intense peak labeled as "VE" was shown at 0.22 eV in Figure 3b, followed by weaker peaks in the high binding energy side akin to a vibrational progression. The R2PD image displays a bright spot in the center (Figure 3a), corresponding to features labeled as "E_{hb}" in the R2PD photoelectron spectrum with a long tail extending to lower binding energies (Figure 3b).

Table 1. Observed DBS Vibrational Peaks in the Photodetachment Spectrum of $9PT^-$, with Their Wavelengths, Energies in cm^{-1}, Shifts Relative to the Ground Vibrational Level, and Assignments

peak	wavelength (nm)	photon energy (cm^{-1})[a]	shift (cm^{-1})	assignment
0	516.25	19370(5)	0	ground vibrational level of the DBS
1	507.74	19695(5)	325	$44'^1$
2	507.25	19714(5)	344	$66'^162'^1$
3	506.51	19743(5)	373	$64'^145'^1$
4	506.06	19760(5)	390	$43'^1/66'^144'^1$
5	505.58	19779(5)	409	$66'^262'^1$
6	504.79	19810(5)	440	$60'^1/65'^245'^1$
7	504.35	19827(5)	457	$65'^164'^163'^1/66'^265'^163'^1/66'^143'^1$
8	504.15	19835(5)	465	$66'^265'^264'^1/66'^465'^2/65'^264'^2$
9	503.50	19861(5)	491	$64'^263'^1/66'^264'^163'^1/66'^463'^1$

[a]Numbers in parentheses indicate the experimental uncertainties in the last digit.

https://doi.org/10.1021/acs.jpca.1c01563
J. Phys. Chem. A 2021, 125, 2967−2976

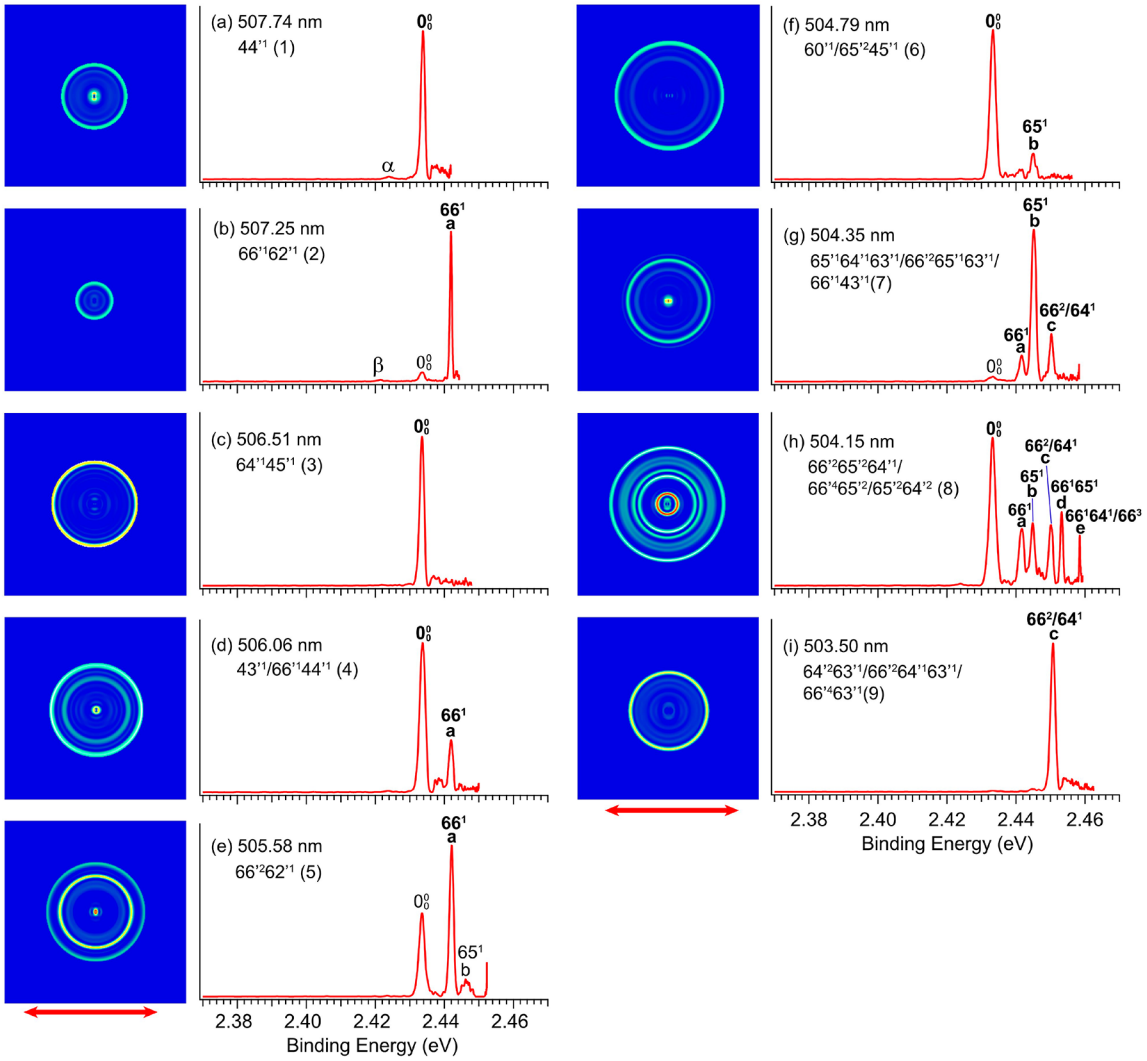

Figure 4. Resonant photoelectron images and spectra of $9PT^-$ at nine wavelengths, corresponding to peaks 1−9 in Figure 2 at (a) 507.74 nm, (b) 507.25 nm, (c) 506.51 nm, (d) 506.06 nm, (e) 505.58 nm, (f) 504.79 nm, (g) 504.35 m, (h) 504.15 nm, and (i) 503.50 nm. The autodetachment-enhanced peaks are labeled in bold face. The vibrational levels of the DBS are also given. The double arrows below the images indicate the direction of the laser polarization.

3.4. Resonant Photoelectron Spectra of $9PT^-$ via the Vibrational Feshbach Resonances. By tuning the detachment laser wavelength to the positions of the above-threshold resonant peaks in Figure 2, we obtained nine resonantly enhanced photoelectron spectra, as shown in Figure 4.

The resonant photoelectron spectra consist of contributions from both nonresonant detachment processes represented by the weak above-threshold baseline in Figure 2 and resonantly enhanced autodetachment via vibrational levels of the DBS. In general, the resonant photoelectron spectra are highly non-Franck−Condon, where one or more vibrational final states are enhanced due to the $\Delta v = -1$ vibrational autodetachment propensity rule.[71,72] The binding energies in eV and cm^{-1}, shifts relative to the 0−0 peak, and the assignments of the observed vibrational peaks are summarized in Table 2.

Table 2. Binding Energies (BE) of the Observed Vibrational Peaks from the Resonant Photoelectron Spectra of $9PT^-$, as Well as Their Shifts from the 0−0 Transition and Assignments[a]

peak	BE (eV)[b]	BE (cm^{-1})[b]	shift (cm^{-1})	assignment	frequencies (theo) (cm^{-1})
0_0^0	2.4334(4)	19627(3)	0		
a	2.4417(4)	19694(3)	67	66^1	68
b	2.4457(8)	19726(6)	99	65^1	93
c	2.4501(7)	19761(6)	134	$66^2/64^1$	140
d	2.4540(5)	19793(4)	166	66^165^1	
e	2.4584(2)	19828(2)	201	66^164^1 / 66^3	

[a]The theoretical frequencies of the relevant vibrational modes of 9PT are also given for comparison (see Table S2). [b]Numbers in parentheses indicate the experimental uncertainties in the last digit.

4. DISCUSSION

4.1. Relaxation from the Ground Vibrational Level of the DBS. In the single-color R2PD photoelectron imaging experiment, the first photon excites the $9PT^-$ anion to the bound ground vibrational level of the DBS at 516.25 nm (19 370 cm^{-1} or 2.4016 eV) and the second photon within the same laser pulse (5 ns pulse width) detaches the dipole-bound electron. The photoelectron image in Figure 3a shows the electron kinetic energy distribution and Figure 3b displays the

https://doi.org/10.1021/acs.jpca.1c01563
J. Phys. Chem. A 2021, 125, 2967−2976

binding energy spectrum obtained by subtracting the electron kinetic energy distribution from the photon energy of the second photon. A single low binding energy peak (labeled as "π-DBS"), corresponding to the outermost ring in Figure 3a, was expected. However, the R2PD photoelectron image and spectrum were much more complicated, suggesting that relaxation processes from the bound DBS (both σ- and π-DBS, *vide infra*) level to other states of the $9PT^-$ anion took place before detachment by the second photon within the same laser pulse, as schematically shown in Figure 5 (the right-hand part of the Figure). Similar R2PD features were also observed in $9AT^-$.[38] Our theoretical calculations predicted a triplet valence excited state at 2.1 eV above the anion ground state (Table S3), i.e., 0.2 eV below the detachment threshold (calculated to be 2.3 eV), in good agreement with the experimental features labeled as "VE" in Figure 3b. This triplet valence excited state was populated due to relaxation from the DBS via intersystem crossing upon absorption of the first photon (Figure 5). Such intersystem crossing from DBSs to valence excited states was first observed previously in the deprotonated biphenol anion.[73]

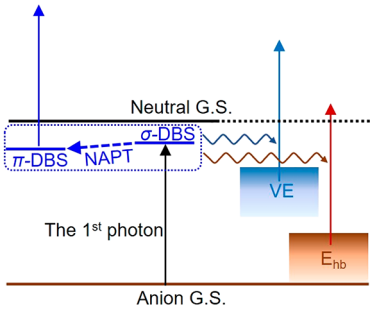

Figure 5. Schematic diagram showing the relaxation processes upon the first photon absorption in the R2PD via the bound ground vibrational level of the DBS of $9PT^-$. VE = valence excited state; E_{hb} = vibrationally excited states of the $9PT^-$ ground state; NAPT = nonadiabatic population transfer.

The bright spot in the center of the image in Figure 3a corresponds to the high binding energy features labeled as "E_{hb}" in Figure 3b, which should be due to detachment from states close to the ground state of $9PT^-$. Since there are no low-lying excited electronic states in $9PT^-$ according to our theoretical calculation, the low kinetic energy electrons must come from detachment from vibrationally excited levels of the ground electronic state of $9PT^-$, via internal conversion from the DBS followed by intramolecular vibrational energy redistribution (IVR).[74] Similar internal conversion processes from nonvalence excited states to the ground electronic states of anions seem to be quite common and have been observed before.[38,53,75,76] Recently, the autodetachment dynamics from vibrational Feshbach resonances of the DBS in the phenoxide anion has been studied using a pump−probe experiment.[77] It is also interesting to directly probe the dynamics of the intersystem crossing and internal conversion from the DBS to valence excited states in anions. These processes are important to understand the anion formation dynamics via DBSs as a doorway state in collision-free environments, such as the interstellar medium.[19−21] In fact, the ultrafast dynamics from DBSs to valence-bound states have been studied in solvated iodide cluster anions following intracluster charge-transfer excitation.[78,79]

4.2. Observation of the π-DBS. The most interesting observation in the R2PD photoelectron image in Figure 3a is the angular distribution of the outermost ring, corresponding to detachment from the vibrational ground state of the DBS by the second photon. The (s + d)-wave distribution, similar to that observed for $9AT^-$,[38] suggests that the DBS has a π symmetry, in contrast to the expected σ symmetry for the lowest DBS as observed in the phenoxide anion and other DBSs that have been studied via photoelectron imaging. The fitted angular anisotropy parameter (β) of the π-DBS peak is −0.3 for $9PT^-$, compared to β = −0.7 for $9AT^-$, whereas β = −1 is expected for a perfect atomic p orbital with the angular momentum quantum number l = 1.[80,81] It should also be noted that the angular distribution of the π-DBS peak is similar to that of the VE peak, which also has a β value of −0.3. The (s + d)-wave angular distribution of the VE peak is consistent with the π^* LUMO of $9PT^-$ (Table S3), from which the electron is detached by the second photon.

4.2.1. Theoretical Description of the DBSs in $9PT^-$. The lowest DBS is expected to be of σ symmetry. A higher energy DBS with π symmetry was predicted to exist for molecular systems with large dipole moments (>9.64 D),[3,28] but was never observed before except in $9AT^-$ recently, in which the anisotropic polarizability was suggested to stabilize the π-DBS.[38] The dipole moment of 9PT is calculated to be 4.4 D, which is far smaller than the calculated critical value for a bound π-type DBS. Hence, a similar mechanism for the stabilization of the π-DBS in $9AT^-$ is expected to be operational in $9PT^-$, even though $9PT^-$ (C_s) has lower symmetry than $9AT^-$ (C_{2v}) (see Figure S1). Our theoretical calculations indeed suggested a bound σ- and a bound π-type DBS in $9PT^-$, as shown in Figure 6. The diffuse orbital of the σ-DBS is found far away from the molecular core and mostly on the positive side of the dipole without any angular node (Figure 6a). On the other hand, the diffuse orbital of the π-DBS is observed on both sides of 9PT, perpendicular to the dipole axis and with an angular node (Figure 6b). While the orbital of the σ-DBS is nearly identical to that in $9AT^-$, that of the π-DBS is significantly asymmetric in contrast to the symmetric π-DBS of $9AT^-$, due to the lower symmetry of $9PT^-$. The asymmetric π-DBS of $9PT^-$ is directly responsible for the smaller anisotropy of the angular distribution observed in the R2PD image of the π-DBS peak for $9PT^-$ (β = −0.3) in comparison to that in $9AT^-$ (β = −0.7).

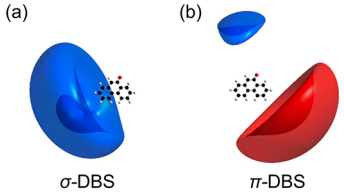

Figure 6. Calculated σ- and π-DBS wave functions of $9PT^-$ (isovalue = 0.003).

To further understand the effects of the molecular structures on the π-DBS, we calculated the components of the polarizability tensor $\boldsymbol{\alpha}$ and the isotropic polarizability α_{iso} of 9PT, as compared with those of 9AT in Table 3. The results show that the isotropic polarizabilities α_{iso} of 9PT (α_{iso} = 174.0) and 9AT (α_{iso} = 178.8) are both large in magnitude and similar to each other, as expected because of their identical size. The large polarizability of 9PT must contribute

https://doi.org/10.1021/acs.jpca.1c01563
J. Phys. Chem. A 2021, 125, 2967−2976

Table 3. Components of the Theoretical Polarizability Tensor α and the Isotropic Polarizability α_{iso} (in Atomic Units) of the Neutral 9PT and 9AT Radicals

polarizability	9PT	9AT
α_{xx}	78.3	78.5
α_{xy}	0.0	0.0
α_{yy}	231.9	284.0
α_{xz}	0.0	0.0
α_{yz}	−31.2	0.0
α_{zz}	211.7	173.7
α_{iso}	174.0	178.8

significantly to the binding energy of the DBS, similar to that in 9AT. The components of the polarizability tensor in the two systems are similar, and are consistent with the molecular symmetries. The dipole axis in $9AT^-$ is perpendicular to the y-axis, and the large α_{yy} component stabilizes the π-DBS along the y-axis (Figure S1). In $9PT^-$, both the large α_{yy} and α_{zz} values should contribute to the stabilization of the π-DBS, resulting in its asymmetry and making it energetically close to or even lower than the σ-DBS.

4.2.2. Population Transfer from the σ-DBS to the π-DBS via Nonadiabatic Coupling. Another interesting question is, how is the π-DBS accessed by the first photon in the R2PD process? For $9AT^-$ with C_{2v} symmetry, the transition from the anion ground state (A_1 symmetry) to the σ-DBS (B_1 symmetry) is dipole-allowed, while that to the π-DBS (A_2 symmetry) is dipole-forbidden.[38,82] Population transfer from the initially excited σ-DBS to the π-DBS was proposed via nonadiabatic coupling. This mechanism suggested that the energy of the π-DBS should be nearly degenerate with or lower in energy than the σ-DBS and the nonadiabatic population transfer (NAPT) was mediated by molecular rotation due to angular momentum conservation. The NAPT mechanism was plausible because most of the $9AT^-$ anions were expected to be in rotationally excited states due to the 30−35 K rotational temperature of the anions from our cryogenically controlled ion trap.[23,54] The lower symmetry of $9PT^-$ (C_s) suggests that the transitions from its ground state (A′ symmetry) to the σ (A″ symmetry) and π (A′ symmetry) DBSs are both dipole-allowed. However, the same NAPT mechanism should still be operational in the R2PD process, because the angular distribution clearly shows that the second photon detaches the electron from the π-DBS, as schematically shown in Figure 5 (left-hand side). The time scale of the NAPT process should be on the order of the rotational period, i.e., picoseconds. Thus, the pump−probe experiment used recently to study the autodetachment dynamics from the vibrational Feshbach resonances of the DBS in phenoxide[77] would be ideal to probe the NAPT dynamics by monitoring the time evolution of the angular distribution of the R2PD photoelectron image.

4.3. Resonant Photoelectron Imaging and Spectra via the Vibrational Feshbach Resonances. Resonant photoelectron spectra at the above-threshold vibrational levels of the DBS are dominated by single-photon excitation followed by vibrational autodetachment, during which the vibrational energy of the neutral core is coupled to the dipole-bound electron. Because the diffuse dipole-bound electron has little effect on the structure of the neutral core, the geometry of the DBS and the corresponding neutral state are almost identical, resulting in the $\Delta v = -1$ propensity rule for the vibrational autodetachment under the harmonic approximation.[71,72] Violation of the $\Delta v = -1$ propensity rule can happen as a result of anharmonicity[71] and has been observed often for low-frequency bending modes.[27,83] Thus, one or more vibrational final states are enhanced in the resonant photoelectron spectra, which are highly non-Franck−Condon. For excitations to combinational or overlapping vibrational levels of the DBS, the resulting resonant photoelectron spectra can be more complicated, rich with vibrational information that would not be assessible in nonresonant PES. Because the autodetachment lifetime (on the order of a few picoseconds as recently measured[77]) is expected to be similar to the time scale of the nonadiabatic population transfer shown in Figure 5, the autodetachment can in principle occur from vibrational levels of the σ-DBS and/or the π-DBS. The current experiment could not distinguish them because the near degeneracy of the σ- and π-DBS and both would produce isotropic angular distributions as observed experimentally (Figure 4) because all the time scales are comparable to the rotational time scale.

Using the autodetachment propensity rule and guided by the calculated frequencies for 9PT (Table S2), we were able to assign all the vibrational levels of the DBS observed in Figure 2, as given in Table 1. Except for peak 1, which is due to the fundamental excitation of mode ν_{44}' ($44'^1$), all other peaks are due to either combinational vibrational levels (peaks 2, 3, 5) or overlapping vibrational levels (peaks 4, 6, 7, 8, 9). The prime ′ is used to designate the vibrational modes and levels of the DBS, even though they are assumed to be the same as the neutral 9PT radical. Because the overtone of the lowest bending mode (ν_{66} = 68 cm^{-1}) is nearly degenerate with the fundamental frequency of mode ν_{64} (140 cm^{-1}, Table S2), a number of higher vibrational levels (peaks 7, 8, 9) contain several possibilities due to the ambiguity between $66'^2$ and $64'^1$. The DBS vibrational levels excited are given in the resonant photoelectron spectra in Figure 4, as well as the excitation wavelengths (see Table 1). The resonant photoelectron spectra contain contributions from both the nonresonant photodetachment processes and autodetachment from resonant excitation to the DBS vibrational levels. However, the autodetachment dominates the resonant photoelectron spectra because the nonresonant photodetachment cross section is much lower, as can be seen by the weak above-threshold baseline in Figure 2. This can also be seen in Figure 4b by the weak 0−0 transition, which is due to the nonresonant detachment process, relative to the intense peak **a** (66^1), which is due to resonant excitation to the $66'^1 62'^1$ DBS vibrational level followed by coupling of the $62'^1$ quantum to the dipole-bound electron. Note here the $66'^1$ quantum (67 cm^{-1}) is not sufficient to detach the dipole-bound electron.

Figure 4a shows the resonant photoelectron spectrum at the photon energy of peak 1 of Figure 2, representing excitation from the ground state of $9PT^-$ to the $44'^1$ vibrational level of the DBS. Transfer of the vibrational energy to the dipole-bound electron via vibronic coupling induces the autodetachment, resulting in the enhanced 0_0^0 peak in Figure 4a. One surprising observation is the weak peak α at 2.4241 eV, which is 75 cm^{-1} below the 0−0 transition due to a vibrational hot band of the $9PT^-$ anion. It should be noted that vibrational population even for the lowest frequency mode in $9PT^-$ should be negligible for the 30−35 K vibrational temperature for our cryogenically cooled anions.[23,55] The unexpected observation of the hot band peak was due to resonant excitation from the

https://doi.org/10.1021/acs.jpca.1c01563
J. Phys. Chem. A 2021, 125, 2967−2976

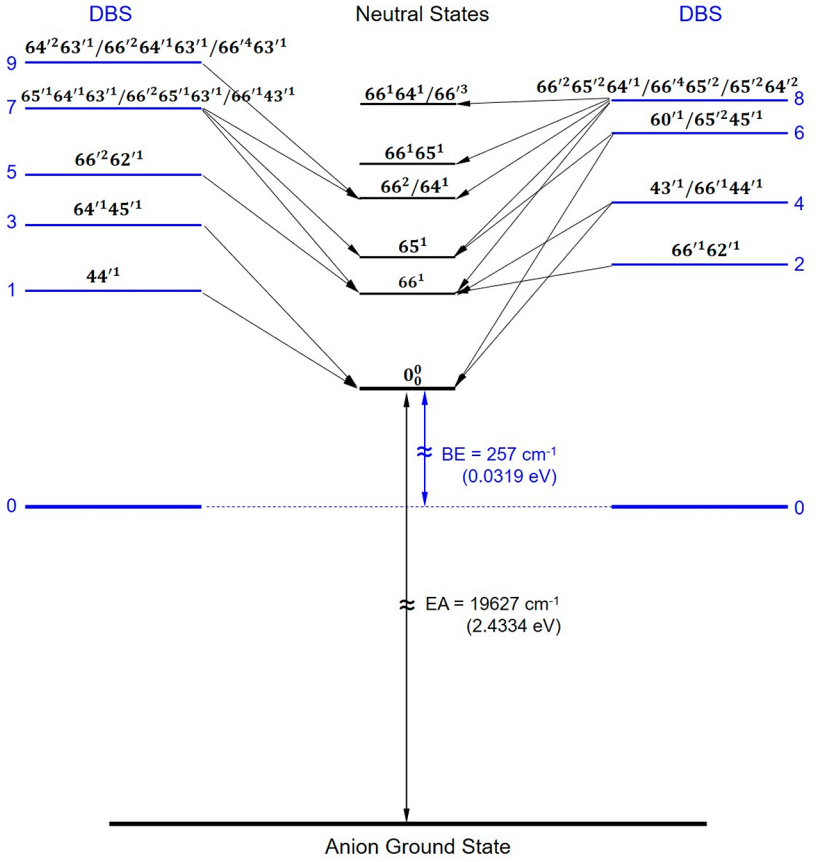

Figure 7. Schematic energy level diagram for autodetachment from the DBS vibrational levels of $9PT^{-}$ to the related neutral final states, corresponding to the nine resonant PE spectra shown in Figure 4.

barely populated vibrational hot band of $9PT^{-}$ to a specific vibrational level of the DBS, followed by autodetachment to the vibrational ground state of the neutral, i.e., a resonantly enhanced hot band transition. In Figure 4a, the resonant excitation is from the 66_a^1 hot band (subscript a is used here to denote the vibrational level of the $9PT^{-}$ anion) to the $43'^1$ level of the DBS. This observation yields a frequency of 75 cm^{-1} for the ν_{66} mode of the $9PT^{-}$ anion. A weak resonantly enhanced hot band β at 2.4216 eV is also observed in Figure 4b, due to resonant excitation from 65_a^1 of $9PT^{-}$ to the $60'^1$ level of the DBS, yielding a frequency of 95 cm^{-1} for the ν_{65} mode of the $9PT^{-}$ anion.

Figure 4c corresponds to excitation to the combinational level $64'^{1}45'^{1}$, which is one of the weakest resonances observed in Figure 2 (peak 3). Since the computed frequency of either ν_{64}' (140 cm^{-1}) or ν_{45}' (242 cm^{-1}) is large enough to detach the dipole-bound electron, the enhanced 0−0 transition is actually due to the coupling of both vibrational quanta to the dipole-bound electron, in violation of the $\Delta v = -1$ propensity rule and consistent with the weak nature of this resonance in the photodetachment spectrum (Figure 2). The violation of the $\Delta v = -1$ propensity rule is also observed in Figure 4e−i. Figure 4d corresponds to excitation at the strongest resonance (peak 4 in Figure 2) to an overlapping vibrational level of $43'^{1}/66'^{1}44'^{1}$. The excitation to the $43'^{1}$ DBS vibrational level resulted in the enhancement of the 0−0 transition, whereas the enhancement of the 66^{1} final vibrational peak was due to excitation to the $66'^{1}44'^{1}$ combinational level, because the sum of the computed ν_{66}' and ν_{44}' frequencies (396 cm^{-1}) is almost exactly the same as that of the ν_{43}' mode (398 cm^{-1}). The other resonant photoelectron spectra in Figure 4 can be readily understood similarly. Figure 4h shows the most complicated resonant photoelectron spectrum due to the excitation to three overlapping vibrational levels all involving in the three lowest frequency bending modes (ν_{66}', ν_{65}', and ν_{64}'). A schematic energy level diagram showing all the DBS vibrational levels and their autodetachment to the relevant neutral levels is displayed in Figure 7, where the EA of 9PT and the binding energy of the DBS are also given. All the observed vibrational peaks and their assignments from the resonant photoelectron spectra are summarized in Table 2.

The combination of the photodetachment spectrum and the resonant photoelectron spectra yielded rich spectroscopic information for the 9PT radical. In addition to the two Franck−Condon active modes (ν_{43} and ν_{44}), we have observed seven Franck−Condon inactive modes, including the six lowest bending modes. Table 4 summarizes all the observed vibrational frequencies for the nine vibrational modes of 9PT, in comparison with the calculated values. The displacement vectors for the nine observed normal modes of vibration for 9PT are shown in Figure S2.

5. CONCLUSION

We report a photodetachment spectroscopy and high-resolution resonant photoelectron imaging study of cryogenically cooled 9-phenanthrolate anions. The electron affinity of the 9-phenanthroxy radical is measured to be 19 627 ± 3 cm^{-1} (2.4334 ± 0.0004 eV). The photodetachment spectrum revealed a dipole-bound excited state 257 cm^{-1} below the detachment threshold of $9PT^{-}$. Resonant two-photon photo-

https://doi.org/10.1021/acs.jpca.1c01563
J. Phys. Chem. A 2021, 125, 2967−2976

Table 4. Measured Vibrational Frequencies for the 9PT Radical in This Work, Compared with the Theoretical Values at the DFT/B3LYP/6-311++(d,p) Level of Theory

vibrational mode	symmetry	theoretical frequency (cm^{-1})	experimental frequency (cm^{-1})[a]
ν_{66}	A″	68	67
ν_{65}	A″	93	99
ν_{64}	A″	140	134
ν_{63}	A″	226	223
ν_{62}	A″	283	277
ν_{60}	A″	443	440
ν_{45}	A′	242	239
ν_{44}	A′	328	325
ν_{43}	A′	398	390

[a]The experimental uncertainty is estimated to be ±3 cm^{-1}.

electron imaging showed that the DBS is of π symmetry, which was shown to be stabilized by the anisotropic polarizability of the 9PT radical similar to that observed in the more symmetric 9-anthrolate anion. The unique π-DBS is suggested to be populated from the initially excited σ-type DBS via non-adiabatic coupling mediated by molecular rotations. Nine above-threshold vibrational resonances (vibrational Feshbach resonances) were also observed for the DBS of $9PT^-$ in the photodetachment spectrum. Highly non-Franck−Condon resonant photoelectron spectra were obtained by tuning the detachment photon energies to the vibrational Feshbach resonances. The combination of the photodetachment spectrum and resonant photoelectron spectra yielded vibrational frequencies for nine vibrational modes of the 9-phenanthroxy radical, including the six lowest frequency bending modes.

■ ASSOCIATED CONTENT

Supporting Information

The Supporting Information is available free of charge at https://pubs.acs.org/doi/10.1021/acs.jpca.1c01563.

Structures of $9PT^-$ and $9AT^-$, nine normal modes of vibration for 9PT observed in the current work, exponents of the diffuse basis functions used in the theoretical calculations, computed frequencies for the 9-phenanthroxy radical, and calculated excitation energy of the triplet excited state of $9PT^-$ and the associated orbitals (PDF)

■ AUTHOR INFORMATION

Corresponding Author

Lai-Sheng Wang − *Department of Chemistry, Brown University, Providence, Rhode Island 02912, United States;* orcid.org/0000-0003-1816-5738; Email: Lai-Sheng_Wang@brown.edu

Authors

Dao-Fu Yuan − *Department of Chemistry, Brown University, Providence, Rhode Island 02912, United States;* orcid.org/0000-0001-8461-6889

Yue-Rou Zhang − *Department of Chemistry, Brown University, Providence, Rhode Island 02912, United States*

Chen-Hui Qian − *Department of Chemistry, Brown University, Providence, Rhode Island 02912, United States*

Yuan Liu − *Department of Chemistry, Brown University, Providence, Rhode Island 02912, United States*

Complete contact information is available at: https://pubs.acs.org/10.1021/acs.jpca.1c01563

Notes

The authors declare no competing financial interest.

■ ACKNOWLEDGMENTS

This work was supported by the Department of Energy, Office of Basic Energy Sciences, Chemical Sciences, Geosciences, and Biosciences Division under Grant DE-SC0018679. The calculation was performed using computational resources and services provided by CCV of Brown University.

■ REFERENCES

(1) Desfrancois, C.; Abdoul-Carmine, H.; Schermann, J. P. Ground-State Dipole-Bound Anions. *Int. J. Mod. Phys. B* **1996**, *10*, 1339−1395.

(2) Compton, R. N.; Hammer, N. I. Multiple-Bound Molecular Anions. *Adv. Gas Phase Ion Chem.* **2001**, *4*, 257−305.

(3) Jordan, K. D.; Wang, F. Theory of Dipole -Bound Anions. *Annu. Rev. Phys. Chem.* **2003**, *54*, 367−396.

(4) Hammer, N. I.; Hinde, R. J.; Compton, R. N.; Diri, K.; Jordan, K. D.; Radisic, D.; Stokes, S. T.; Bowen, K. H. Dipole-Bound Anions of Highly Polar Molecules: Ethylene Carbonate and Vinylene Carbonate. *J. Chem. Phys.* **2004**, *120*, 685−690.

(5) Simons, J. Molecular Anions. *J. Phys. Chem. A* **2008**, *112*, 6401−6511.

(6) Marks, J.; Comita, P. B.; Brauman, J. I. Threshold Resonances in Electron Photodetachment Spectra. Structural Evidence for Dipole-Supported States. *J. Am. Chem. Soc.* **1985**, *107*, 3718−3719.

(7) Lykke, K. R.; Mead, R. D.; Lineberger, W. C. Observation of Dipole-Bound States of Negative Ions. *Phys. Rev. Lett.* **1984**, *52*, 2221−2224.

(8) Mead, R. D.; Lykke, K. R.; Lineberger, W. C.; Marks, J.; Brauman, J. I. Spectroscopy and Dynamics of the Dipole-Bound State of Acetaldehyde Enolate. *J. Chem. Phys.* **1984**, *81*, 4883−4892.

(9) Yokoyama, K.; Leach, G. W.; Kim, J. B.; Lineberger, W. C.; Boldyrev, A. I.; Gutowski, M. Autodetachment Spectroscopy and Dynamics of Vibrationally Excited Dipole-Bound States of H_2CCC^-. *J. Chem. Phys.* **1996**, *105*, 10706−10718.

(10) Dessent, C. E. H.; Kim, J.; Johnson, M. A. Photochemistry of Halide Ion−Molecule Clusters: Dipole-Bound Excited States and the Case for Asymmetric Solvation. *Acc. Chem. Res.* **1998**, *31*, 527−534.

(11) Dao, D. B.; Mabbs, R. The Effect of the Dipole Bound State on AgF^- Vibrationally Resolved Photodetachment Cross Sections and Photoelectron Angular Distributions. *J. Chem. Phys.* **2014**, *141*, 154304.

(12) Mascaritolo, K. J.; Gardner, A. M.; Heaven, M. C. Autodetachment Spectroscopy of the Aluminum Oxide Anion Dipole Bound State. *J. Chem. Phys.* **2015**, *143*, 114311.

(13) Castellani, M. E.; Anstoter, C. S.; Verlet, J. R. R. On the Stability of a Dipole-Bound State in the Presence of a Molecule. *Phys. Chem. Chem. Phys.* **2019**, *21*, 24286−24290.

(14) Compton, R. N.; Carman, H. S.; Desfrancois, C.; Abdoul-Carime, H.; Schermann, J. P.; Hendricks, J. H.; Lyapustina, S. A.; Bowen, K. H. On the Binding of Electrons to Nitromethane: Dipole and Valence Bound Anions. *J. Chem. Phys.* **1996**, *105*, 3472−3478.

(15) Mikulski, P.; Klahn, T.; Krebs, P. Excess Electron Mobility in Low Density CH_3CN Gas: Short-Lived Dipole-Bound Electron Ground States as Precursors of Localized Electron States. *Phys. Rev. A: At., Mol., Opt. Phys.* **1997**, *55*, 369−377.

(16) Sommerfeld, T. Coupling between Dipole-Bound and Valence States: The Nitromethane Anion. *Phys. Chem. Chem. Phys.* **2002**, *4*, 2511−2516.

(17) Burrow, P. D.; Gallup, G. A.; Scheer, A. M.; Denifl, S.; Ptasinska, S.; Mark, T.; Scheier, P. Vibrational Feshbach Resonances in Uracil and Thymine. *J. Chem. Phys.* **2006**, *124*, 124310.

(18) Boudaiffa, B.; Cloutier, P.; Hunting, D.; Huels, M. A.; Sanche, L. Resonant Formation of DNA Strand Breaks by Low-Energy (3 to 20 eV) Electrons. *Science* **2000**, *287*, 1658−1660.
(19) Sarre, P. J. The Diffuse Interstellar Bands: A Dipole-Bound State Hypothesis. *Mon. Not. R. Astron. Soc.* **2000**, *313*, L14−L16.
(20) Fortenberry, R. C.; Crawford, T. D. Theoretical Prediction of New Dipole-Bound Singlet States for Anions of Interstellar Interest. *J. Chem. Phys.* **2011**, *134*, 154304.
(21) Fortenberry, R. C. Interstellar Anions: The Role of Quantum Chemistry. *J. Phys. Chem. A* **2015**, *119*, 9941−9953.
(22) Liu, H. T.; Ning, C. G.; Huang, D. L.; Dau, P. D.; Wang, L. S. Observation of Mode-Specific Vibrational Autodetachment from Dipole-Bound States of Cold Anions. *Angew. Chem., Int. Ed.* **2013**, *52*, 8976−8979.
(23) Liu, H. T.; Ning, C. G.; Huang, D. L.; Wang, L. S. Vibrational Spectroscopy of the Dehydrogenated Uracil Radical via Autodetachment of Dipole-Bound Excited States of Cold Anions. *Angew. Chem., Int. Ed.* **2014**, *53*, 2464−2468.
(24) Huang, D. L.; Liu, H. T.; Ning, C. G.; Wang, L. S. Vibrational State-Selective Autodetachment Photoelectron Spectroscopy from Dipole-Bound States of Cold 2-Hydroxyphenoxide: *o*-HO$(C_6H_4)O^-$. *J. Chem. Phys.* **2015**, *142*, 124309.
(25) Huang, D. L.; Liu, H. T.; Ning, C. G.; Zhu, G. Z.; Wang, L. S. Probing the Vibrational Spectroscopy of the Deprotonated Thymine Radical by Photodetachment and State-Selective Autodetachment Photoelectron Spectroscopy via Dipole-Bound States. *Chem. Sci.* **2015**, *6*, 3129−3138.
(26) Zhu, G. Z.; Huang, D. H.; Wang, L. S. Conformation-Selective Resonant Photoelectron Imaging from Dipole-Bound States of Cold 3-Hydroxyphenoxide. *J. Chem. Phys.* **2017**, *147*, 013910.
(27) Zhu, G. Z.; Wang, L. S. High-Resolution Photoelectron Imaging and Resonant Photoelectron Spectroscopy via Noncovalent-Bound Excited States of Cryogenically-Cooled Anions. *Chem. Sci.* **2019**, *10*, 9409−9423.
(28) Wallis, R. F.; Herman, R.; Milnes, H. W. Energy Levels of an Electron in the Field of a Finite Dipole. *J. Mol. Spectrosc.* **1960**, *4*, 51−74.
(29) Turner, J. E. Minimum Dipole Moment Required to Bind an Electron − Molecular Theorists Rediscover Phenomenon Mentioned in Fermi-Teller Paper Twenty Years Earlier. *Am. J. Phys.* **1977**, *45*, 758−766.
(30) Crawford, O. H.; Garrett, W. R. Electron-Affinities of Polar-Molecules. *J. Chem. Phys.* **1977**, *66*, 4968−4970.
(31) Garrett, W. R. Critical Binding of an Electron by a Nonstationary, Point-Dipole Rotor. *Phys. Rev. A: At., Mol., Opt. Phys.* **1980**, *22*, 1769−1770.
(32) Desfrançois, C.; Abdoul-Carime, H.; Khelifa, N.; Schermann, J. P. From $1/r$ to $1/r^2$ Potentials: Electron Exchange between Rydberg Atoms and Polar Molecules. *Phys. Rev. Lett.* **1994**, *73*, 2436−2439.
(33) Hammer, N. I.; Diri, K.; Jordan, K. D.; Desfrançois, C.; Compton, R. N. Dipole-Bound Anions of Carbonyl, Nitrile, and Sulfoxide Containing Molecules. *J. Chem. Phys.* **2003**, *119*, 3650−3660.
(34) Qian, C. H.; Zhu, G. Z.; Wang, L. S. Probing the Critical Dipole Moment to Support Excited Dipole-Bound States in Valence-Bound Anions. *J. Phys. Chem. Lett.* **2019**, *10*, 6472−6477.
(35) Garrett, W. R. Critical Binding of Electron−Dipole Rotor Systems; Electronically Excited States. *J. Chem. Phys.* **1980**, *73*, 5721−5725.
(36) Garrett, W. R. Excited States of Polar Negative Ions. *J. Chem. Phys.* **1982**, *77*, 3666−3673.
(37) Huang, D. L.; Zhu, G. Z.; Liu, Y.; Wang, L. S. Photodetachment Spectroscopy and Resonant Photoelectron Imaging of Cryogenically-Cooled Deprotonated 2-Hydroxypyrimidine Anions. *J. Mol. Spectrosc.* **2017**, *332*, 86−93.
(38) Yuan, D. F.; Liu, Y.; Qian, C. H.; Zhang, Y. R.; Rubenstein, B. M.; Wang, L. S. Observation of a π-Type Dipole-Bound State in Molecular Anions. *Phys. Rev. Lett.* **2020**, *125*, 073003.
(39) Chagger, H.K; Jones, J.M; Pourkashanian, M; Williams, A; Owen, A; Fynes, G Emission of Volatile Organic Compounds from Coal Combustion. *Fuel* **1999**, *78*, 1527−1538.
(40) Guinamard, R.; Hof, T.; Del Negro, C. A. The TRPM4 Channel Inhibitor 9-Phenanthrol. *Br. J. Pharmacol.* **2014**, *171*, 1600−1613.
(41) Mansurov, Z. A. Soot Formation in Combustion Processes. *Combust., Explos. Shock Waves* **2005**, *41*, 727−744.
(42) Neumark, D. M. Slow Electron Velocity-Map Imaging of Negative Ions: Applications to Spectroscopy and Dynamics. *J. Phys. Chem. A* **2008**, *112*, 13287−13301.
(43) Weichman, M. L.; Neumark, D. M. Slow Electron Velocity-Map Imaging of Cryogenically Cooled Anions. *Annu. Rev. Phys. Chem.* **2018**, *69*, 101−124.
(44) Kim, J. B.; Weichman, M. L.; Yacovitch, T. I.; Shih, C.; Neumark, D. M. Slow Photoelectron Velocity-Map Imaging Spectroscopy of the C_9H_7 (Indenyl) and $C_{13}H_9$ (Fluorenyl) Anions. *J. Chem. Phys.* **2013**, *139*, 104301.
(45) Weichman, M. L.; Kim, J. B.; DeVine, J. A.; Levine, D. S.; Neumark, D. M. Vibrational and Electronic Structure of the α- and β-Naphthyl Radicals via Slow Photoelectron Velocity-Map Imaging. *J. Am. Chem. Soc.* **2015**, *137*, 1420−1423.
(46) Weichman, M. L.; DeVine, J. A.; Levine, D. S.; Kim, J. B.; Neumark, D. M. Isomer-Specific Vibronic Structure of the 9-, 1-, and 2-Anthracenyl Radicals via Slow Photoelectron Velocity-Map Imaging. *Proc. Natl. Acad. Sci. U. S. A.* **2016**, *113*, 1698−1705.
(47) Kregel, S. J.; Thurston, G. K.; Garand, E. Photoelectron Spectroscopy of Anthracene and Fluoranthene Radical Anions. *J. Chem. Phys.* **2018**, *148*, 234306.
(48) Kregel, S. J.; Garand, E. Ground and Low-Lying Excited States of Phenoxy, 1-Naphthoxy, and 2-Naphthoxy Radicals via Anion Photoelectron Spectroscopy. *J. Chem. Phys.* **2018**, *149*, 074309.
(49) Wang, L. S.; Ding, C. F.; Wang, X. B.; Barlow, S. E. Photodetachment Photoelectron Spectroscopy of Multiply Charged Anions Using Electrospray Ionization. *Rev. Sci. Instrum.* **1999**, *70*, 1957−1966.
(50) Wang, X. B.; Wang, L. S. Development of a Low-Temperature Photoelectron Spectroscopy Instrument Using an Electrospray Ion Source and a Cryogenically Controlled Ion Trap. *Rev. Sci. Instrum.* **2008**, *79*, 073108.
(51) León, I.; Yang, Z.; Liu, H. T.; Wang, L. S. The Design and Construction of a High-Resolution Velocity-Map Imaging Apparatus for Photoelectron Spectroscopy Studies of Size-Selected Clusters. *Rev. Sci. Instrum.* **2014**, *85*, 083106.
(52) Wang, L. S. Electrospray Photoelectron Spectroscopy: From Multiply-Charged Anions to Ultracold Anions. *J. Chem. Phys.* **2015**, *143*, 040901.
(53) Qian, C.-H.; Zhu, G.-Z.; Zhang, Y.-R.; Wang, L.-S. Photodetachment Spectroscopy and Resonant Photoelectron Imaging of the 2-Naphthoxide Anion via Dipole-Bound Excited States. *J. Chem. Phys.* **2020**, *152*, 214307.
(54) Qian, C. H.; Zhang, Y. R.; Yuan, D. F.; Wang, L. S. Photodetachment Spectroscopy and Resonant Photoelectron Imaging of Cryogenically-Cooled 1-Pyrenolate. *J. Chem. Phys.* **2021**, *154*, 094308.
(55) Huang, D. L.; Zhu, G. Z.; Wang, L. S. Observation of Dipole-Bound State and High-Resolution Photoelectron Imaging of Cold Acetate Anions. *J. Chem. Phys.* **2015**, *142*, 091103.
(56) Garcia, G. A.; Nahon, L.; Powis, I. Two-Dimensional Charged Particle Image Inversion Using a Polar Basis Function Expansion. *Rev. Sci. Instrum.* **2004**, *75*, 4989−4996.
(57) Dribinski, V.; Ossadtchi, A.; Mandelshtam, V. A.; Reisler, H. Reconstruction of Abel-Transformable Images: The Gaussian Basis-Set Expansion Abel Transform Method. *Rev. Sci. Instrum.* **2002**, *73*, 2634−2642.
(58) Becke, A. D. Density-functional Thermochemistry. III. The Role of Exact Exchange. *J. Chem. Phys.* **1993**, *98*, 5648−5652.
(59) Lee, C.; Yang, W.; Parr, R. G. Development of the Colle-Salvetti Correlation-Energy Formula into a Functional of the Electron

https://doi.org/10.1021/acs.jpca.1c01563
J. Phys. Chem. A 2021, 125, 2967−2976

Density. *Phys. Rev. B: Condens. Matter Mater. Phys.* **1988**, *37*, 785−789.
(60) Miehlich, B.; Savin, A.; Stoll, H.; Preuss, H. Results Obtained with the Correlation Energy Density Functionals of Becke and Lee, Yang and Parr. *Chem. Phys. Lett.* **1989**, *157*, 200−206.
(61) Weigend, F. Accurate Coulomb-Fitting Basis Sets for H to Rn. *Phys. Chem. Chem. Phys.* **2006**, *8*, 1057−1065.
(62) Weigend, F.; Ahlrichs, R. Balanced Basis Sets of Split Valence, Triple Zeta Valence and Quadruple Zeta Valence Quality for H to Rn: Design and Assessment of Accuracy. *Phys. Chem. Chem. Phys.* **2005**, *7*, 3297−3305.
(63) Bauernschmitt, R.; Ahlrichs, R. Treatment of Electronic Excitations within the Adiabatic Approximation of Time Dependent Density Functional Theory. *Chem. Phys. Lett.* **1996**, *256*, 454−464.
(64) Casida, M. E.; Jamorski, C.; Casida, K. C.; Salahub, D. R. Molecular Excitation Energies to High-Lying Bound States from Time-Dependent Density-Functional Response Theory: Characterization and Correction of the Time-Dependent Local Density Approximation Ionization Threshold. *J. Chem. Phys.* **1998**, *108*, 4439−4449.
(65) Stratmann, R. E.; Scuseria, G. E.; Frisch, M. J. An Efficient Implementation of Time-Dependent Density-Functional Theory for the Calculation of Excitation Energies of Large Molecules. *J. Chem. Phys.* **1998**, *109*, 8218−8224.
(66) Yanai, T.; Tew, D. P.; Handy, N. C. A New Hybrid Exchange−Correlation Functional Using the Coulomb-Attenuating Method (CAM-B3LYP). *Chem. Phys. Lett.* **2004**, *393*, 51−57.
(67) Frisch, M. J.; Trucks, G. W.; Schlegel, H. B.; Scuseria, G. E.; Robb, M. A.; Cheeseman, J. R.; Scalmani, G.; Barone, V.; Petersson, G. A.; Nakatsuji, H.; et al. *Gaussian 09*, Revision D.01; Gaussian, Inc.: Wallingford, CT, 2016.
(68) Pugliesi, I.; Müller-Dethlefs, K. The Use of Multidimensional Franck−Condon Simulations to Assess Model Chemistries: A Case Study on Phenol. *J. Phys. Chem. A* **2006**, *110*, 4657−4667.
(69) Huang, D. L.; Liu, H. T.; Ning, C. G.; Wang, L. S. Conformation-Selective Resonant Photoelectron Spectroscopy via Dipole-Bound States of Cold Anions. *J. Phys. Chem. Lett.* **2015**, *6*, 2153−2157.
(70) Zhu, G. Z.; Qian, C. H.; Wang, L. S. Dipole-Bound Excited States and Resonant Photoelectron Imaging of Phenoxide and Thiophenoxide Anions. *J. Chem. Phys.* **2018**, *149*, 164301.
(71) Berry, R. S. Ionization of Molecules at Low Energies. *J. Chem. Phys.* **1966**, *45*, 1228−1245.
(72) Simons, J. Propensity Rules for Vibration-Induced Electron Detachment of Anions. *J. Am. Chem. Soc.* **1981**, *103*, 3971−3976.
(73) Zhu, G. Z.; Cheung, L. F.; Liu, Y.; Qian, C. H.; Wang, L. S. Resonant Two-Photon Photoelectron Imaging and Intersystem Crossing from Excited Dipole-Bound States of Cold Anions. *J. Phys. Chem. Lett.* **2019**, *10*, 4339−4344.
(74) Freed, K. F.; Nitzan, A. Intramolecular Vibrational Energy Redistribution and the Time Evolution of Molecular Fluorescence. *J. Chem. Phys.* **1980**, *73*, 4765−4778.
(75) Yuan, D. F.; Liu, Y.; Qian, C. H.; Kocheril, G. S.; Zhang, Y. R.; Rubenstein, B. M.; Wang, L. S. Polarization of Valence Orbitals by the Intramolecular Electric Field from a Diffuse Dipole-Bound Electron. *J. Phys. Chem. Lett.* **2020**, *11*, 7914−7919.
(76) Liu, Y.; Zhu, G. Z.; Yuan, D. F.; Qian, C. H.; Zhang, Y. R.; Rubenstein, B. M.; Wang, L. S. Observation of a Symmetry-Forbidden Excited Quadrupole-Bound State. *J. Am. Chem. Soc.* **2020**, *142*, 20240−20246.
(77) Kang, D. H.; An, S.; Kim, S. K. Real-Time Autodetachment Dynamics of Vibrational Feshbach Resonances in a Dipole-Bound State. *Phys. Rev. Lett.* **2020**, *125*, 093001.
(78) Yandell, M. A.; King, S. B.; Neumark, D. M. Decay Dynamics of Nascent Acetonitrile and Nitromethane Dipole-Bound Anions Produced by Intracluster Charge-Transfer. *J. Chem. Phys.* **2014**, *140*, 184317.
(79) King, S. B.; Yandell, M. A.; Stephansen, A. B.; Neumark, D. M. Time-Resolved Radiation Chemistry: Dynamics of Electron Attachment to Uracil Following UV Excitation of Iodide-Uracil Complexes. *J. Chem. Phys.* **2014**, *141*, 224310.
(80) Cooper, J.; Zare, R. N. Angular Distribution of Photoelectrons. *J. Chem. Phys.* **1968**, *48*, 942−943.
(81) Sanov, A. Laboratory-Frame Photoelectron Angular Distributions in Anion Photodetachment: Insight into Electronic Structure and Intermolecular Interactions. *Annu. Rev. Phys. Chem.* **2014**, *65*, 341−363.
(82) Harris, D. C.; Bertolucci, M. D. *Symmetry and Spectroscopy: An Introduction to Vibrational and Electronic Spectroscopy*; Dover Publications Inc.: New York, 1989.
(83) Huang, D. L.; Liu, H. T.; Ning, C. G.; Dau, P. D.; Wang, L. S. Resonant Photoelectron Imaging of Deprotonated Uracil Anion via Vibrational Levels of a Dipole-Bound Excited State. *Chem. Phys.* **2017**, *482*, 374−383.

https://doi.org/10.1021/acs.jpca.1c01563
J. Phys. Chem. A 2021, 125, 2967−2976